JOURNAL OF APPLIED PHYSICS **97**, 044313 (2005)

Morphological and magnetic properties of carbon–nickel nanocomposite thin films

F. C. Fonseca[a]
CCTM-Instituto de Pesquisas Energéticas e Nucleares, Av. Prof. Lineu Prestes 2242, 05508-000 São Paulo, SP, Brazil

A. S. Ferlauto and F. Alvarez
Instituto de Física "Gleb Wataghin," Universidade Estadual de Campinas, CP 6165, 13083-970 Campinas, SP, Brazil

G. F. Goya and R. F. Jardim
Instituto de Física, Universidade de São Paulo, CP 66318, 05315-970 São Paulo, SP, Brazil

(Received 17 May 2004; accepted 7 December 2004; published online 26 January 2005)

Carbon–nickel nanocomposite thin films were prepared by ion beam cosputtering a graphite target having a nickel chip attached to its surface. The amount of Ni incorporated in the films was controlled by the size of the Ni chip (from 5 to 22 wt %), and measured by *in situ* x-ray photoelectron spectroscopy (XPS). High-resolution transmission electron microscopy images indicated that the films have a granular structure with nanosize Ni particles embedded in an amorphous carbon matrix. The Ni particles have an average radius of ∼2 nm, with a rather narrow size distribution. Magnetization measurements revealed that films are superparamagnetic and present blocking temperatures $T_B < 13$ K. The combined results of XPS and magnetic measurements indicate that Ni particles are free from oxide layers. In addition, the estimated value of their anisotropy constant was found to be higher than the expected value for bulk Ni. The origin of this discrepancy is associated with both shape and interaction anisotropies. © *2005 American Institute of Physics*. [DOI: 10.1063/1.1852702]

INTRODUCTION

Nanosize particles (NPs) of ferromagnetic metals such as Fe, Co, and Ni have been extensively studied due to the richness of their physical properties and the wide range of potential applications, including catalysts, high density magnetic recording media, ferrofluids, and medical diagnostics.[1] Metallic NPs can be easily prepared by a number of methods, including evaporation, sputtering, high-energy ball milling, ion exchange, and sol–gel.[2–5] However, the particle size distribution and average size strongly depend on the preparation parameters and methods. In addition, these NPs are highly reactive due to the large surface area to volume ratio and can be easily environmentally degraded. In particular, oxide surface layers can be formed resulting in a shell-core morphology wherein an antiferromagnetic (AFM) oxide layer surrounds the ferromagnetic (FM) metallic NP. Such morphology influences the magnetic properties due to the exchange interaction between the FM and AFM phases. As a consequence, two main challenges remain for the viable application of such NPs: effective control of particle size and protection from oxidation and chemical degradation.

A favored approach to assemble and maintain metallic NPs is to form nanocomposites whereby the NPs are embedded in a nonmagnetic matrix that provides mechanical and chemical stability.[6] Oxides such as silica and alumina have been extensively used as a matrix to provide good magnetic and electric insulation. However, these oxides lack the mechanical and tribological properties required in magnetic storage device applications such as hard disks. On the other hand, carbon-based thin films such as diamond-like carbon and amorphous carbon nitride alloys are widely applied to protect the active magnetic layers in magnetic storage devices, due to their excellent mechanical and tribological characteristics.[7] In this sense, an interesting approach for magnetic storage device production would be to employ carbon-based thin films for metallic NP hosting, thus combining both the active magnetic and protective layers in a single one.

Although there have been previous reports of thin films composed of metallic particles having small dimensions (<10 nm), embedded in disordered carbon matrices,[8] only few studies have investigated the magnetic properties of such structures.[9,10] In this work, the ion beam cosputtering method was used to produce carbon–Ni nanocomposite thin films that present superparamagnetic behavior. The samples were characterized via several techniques including high-resolution transmission electron microscopy (HRTEM), x-ray photoemission spectroscopy (XPS), magnetization $M(T,H)$, and frequency dependent ac magnetic susceptibility $\chi(T,f)$. The results indicate that the C–Ni nanocomposites films are comprised of small Ni particles, having an average radius of <3 nm, embedded in an amorphous carbon matrix. From the combined results of XPS and $M(T,H)$ we have inferred that the Ni nanoparticles are free from a surrounding

---

[a] Author to whom correspondence should be addressed; electronic mail: cfonseca@ipen.br

oxide layer. In addition, the ac magnetic data indicate that the samples could be classified as superparamagnetic systems.

EXPERIMENT

Carbon–nickel composite (C–Ni) films were prepared by the ion beam cosputtering method. Details of the apparatus are described elsewhere.[11] Briefly, in this method, a 3 cm diam Kaufman source generates a 1500 eV argon ion (Ar^+) beam that is directed towards a high-purity graphite target. Small Ni chips are attached to the pure C (99.9999%) target with a carbon-based cement. The relative Ni concentration in the films is controlled by the relative area of Ni pellets exposed to the Ar^+ beam. Due to the much larger sputter yields of Ni as compared to C, this relative area of Ni exposed to the ion beam is small. The resulting sputtered C and Ni atoms were deposited on polished Si wafers heated to 350 °C. This temperature was chosen in order to provide enough thermal energy for the surface and bulk diffusion of the Ni atoms during film growth, therefore promoting the formation of crystalline Ni particles. Pure carbon films produced under similar conditions in our system present a disordered structure wherein the C atoms form mainly sp^2 hybridized bonds.[11] Even though such disordered graphitic structure is not particularly hard, the mechanical properties of the resulting films can be easily optimized, for example, by incorporating nitrogen.[11] The thickness of the studied films was ~500 nm, as measured by profilometry.

The deposited films were transferred *in situ* (with no vacuum break) to an ultrahigh vacuum chamber attached to the deposition system for XPS. The XPS spectra were collected by using the Al K_α line and a cylindrical mirror analyzer, having an overall energy resolution of ~1.2 eV (linewidth plus analyzer). The morphology of the films was examined by HRTEM, using a JEM 3010 URP with 1.7 Å point resolution. The (C–Ni film)/(Si substrate) structures were thinned down by standard polishing and ion milling procedures in order to perform the HRTEM images (top view). Magnetization measurements $M(T,H)$ and frequency dependent ac magnetic susceptibility $\chi(T,f)$ were performed in the as-grown samples by using a superconducting quantum interference device magnetometer with applied magnetic fields H between 0 and 7 T and temperatures ranging from 2 to 350 K. For ac magnetic susceptibility $\chi(T,f)$ measurements we have used an excitation field of 2 Oe and driving frequencies $0.02 \leq f \leq 1300$ Hz. In these experiments, the sample is first cooled down to 5 K under zero applied field, the magnetic field is set and the magnetization data are collected upon warming up to 350 K zero field colled (ZFC), then the data is collected upon cooling the sample down to 5 K (FC). In the $M(H)$ experiments the sample is ZFC cooled down to the desired measuring temperature and the magnetic field sweep ($-7\ \text{T} \leq H \leq 7\ \text{T}$) is performed. These steps were repeated for several different measuring temperatures.

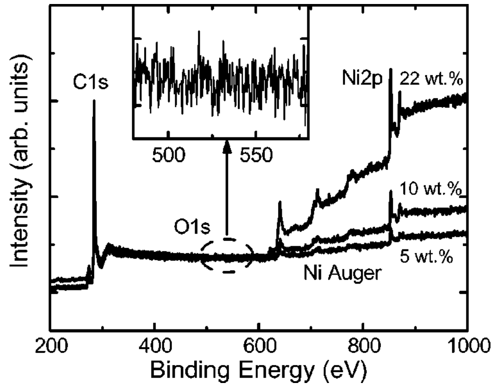

FIG. 1. X-ray photoemission spectroscopy results for the C–Ni films with Ni concentrations of 5, 10, and 22 wt %. The inset shows an expanded view of the oxygen 1*s* energy region (520–530 eV).

RESULTS AND DISCUSSION

The composition of the studied films was determined from *in situ* XPS. The full energy range XPS spectra are depicted in Fig. 1. The only peaks observed in the spectra arise from C 1*s* and Ni 2*p* core electrons and Ni Auger electrons, and contributions from spurious elements were not detected. In particular, no contribution arising from oxygen (O 1*s* electrons) can be distinguished from the inelastic background within the 520–530 eV range, as shown in the inset. Such result indicates that any contamination from oxygen should be less than ~0.5 at. %. The Ni concentration in the films ranged from 5 to 22 wt %. It was determined from the XPS spectra of the individual C 1*s* and Ni 2*p* peaks, by weighting the peak integrated areas with the respective photoionization cross sections.

The structure and morphology of the films were analyzed by HRTEM, as shown in Fig. 2. This figure displays bright-field images, with different magnifications, of two C–Ni films with 10 wt % [Fig. 2(c)] and 22 wt % of Ni [Figs. 2(a) and 2(b)]. The image in Fig. 2(a) indicates that the films have a granular structure, whereby the Ni nanoparticles are clearly discerned as darker regions. These dark regions are surrounded by the disordered carbon matrix (lighter regions). The figures also reveal that the Ni nanoparticles are homogeneously distributed over the carbon matrix and are well separated from each other (see Fig. 2). In addition, it is observed that the Ni nanoparticles have a nearly spherical shape with average diameter close to 4 nm. Images of selective area diffraction (not shown) revealed a pattern of well-defined rings that can be associated with randomly oriented, small size crystalline Ni particles. The crystalline character of the Ni NPs is also confirmed in Figs. 2(b) and 2(c) by the presence of the lattice planes in the NPs. HRTEM images of films with different Ni concentrations indicate that their morphology is essentially unaltered within the range of Ni concentration studied.

In order to determine the NP size distribution, HRTEM images such as the ones of Fig. 2 were digitally processed by using segmentation algorithms. In this procedure, the contour of each NP is identified, thus allowing the distinction of the NPs from the amorphous C matrix. As a result, the projected area of each NP can be determined.[12] The results of a statis-

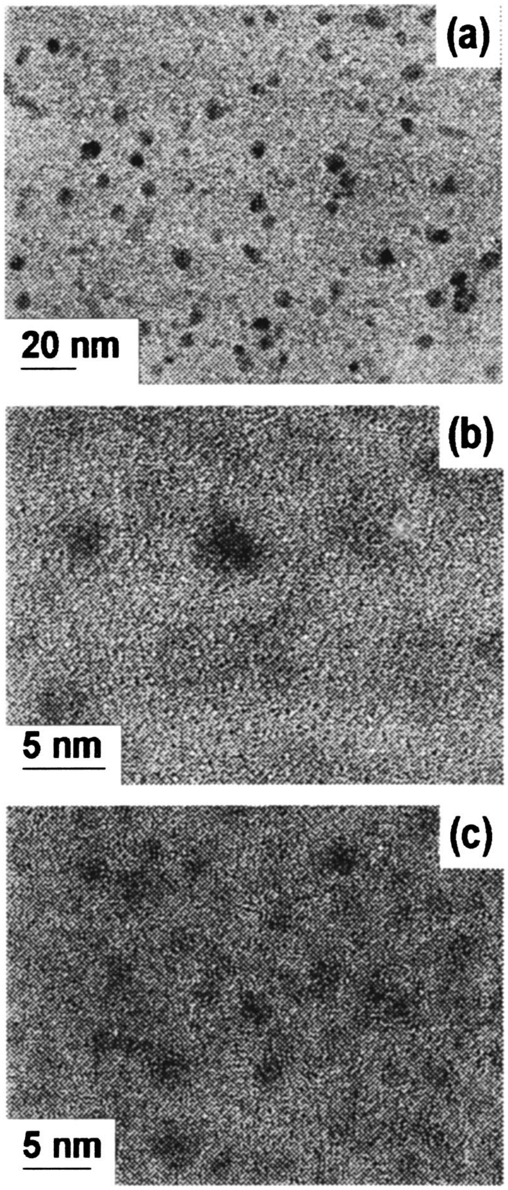

FIG. 2. High resolution transmission electron microscopy images of C–Ni film:. (a) Ni=22 wt % (20 nm scale bar), (b) Ni=22 wt % (5 nm scale bar), and (c) Ni=10 wt % (5 nm scale bar).

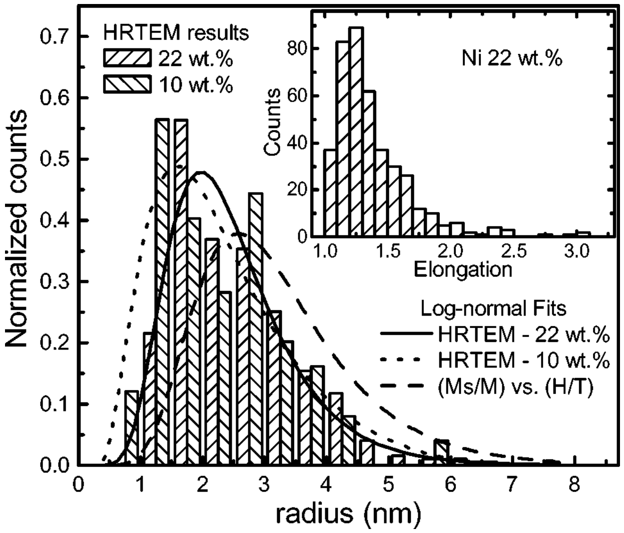

FIG. 3. Size distributions of Ni nanoparticles determined from HRTEM analysis for the C–Ni films with 10 and 22 wt % of Ni. The figure also displays the fitted log-normal distributions for the obtained size distributions and the $M(H,T)$ data analysis. The inset shows the elongation distribution of Ni nanoparticles for the C–Ni film with 22 wt % of Ni.

tical analysis of ~400 particles for the films with 10 and 22 wt % of Ni are depicted in Fig. 3. The columns represent the frequency histogram as a function of the estimated NP radius by assuming that the NPs have spherical shape. The size distributions were found to be well described by a log-normal distribution in agreement with other metallic nanoparticle systems.[13,14] In fact, the particle size distribution for the film with 22 wt % of Ni is rather narrow and displays a maximum at the radius $r_{\mathrm{TEM}}=2.3\pm0.2$ nm and width $\sigma=0.39\pm0.07$ nm. The corresponding results for the film with 10 wt % of Ni were $r_{\mathrm{TEM}}=2.2\pm0.2$ nm and width $\sigma=0.56\pm0.09$ nm. Deviations from the spherical shape were also estimated by adjusting an ellipsoid to the projected area of each NP. In this way, an elongation factor could be determined, defined as the ratio between the major and minor axis of the adjusted contour ellipse. The inset of Fig. 3 displays the elongation distribution for the Ni NPs in the film with 22 wt % of Ni. Such distribution exhibits a pronounced maximum at ~1.2, further confirming the assumed nearly spherical morphology of Ni nanoparticles (see Fig. 2).

The magnetic properties of the studied nanocomposites were also investigated. Hereafter, we will focus the discussion on the results obtained in the sample with the highest concentration of magnetic phase, i.e., the film with 22 wt % of Ni. At this Ni concentration, the magnetic contribution arising from the Ni NPs can be easily discerned from the magnetic contributions of the Si substrate and the amorphous carbon matrix. The temperature dependence of the magnetization measured under both FC and ZFC processes and under two applied magnetic fields of $H=50$ and 100 Oe is shown in Fig. 4. The curves exhibit the expected features of superparamagnetic (SPM) systems: (1) the ZFC curves have a rounded maximum at $T_B\sim 13$ K (see inset of Fig. 4), indicating the occurrence of a blocking process of the Ni NPs and (2) a paramagnetic-like behavior in the temperature range $T>T_B$.

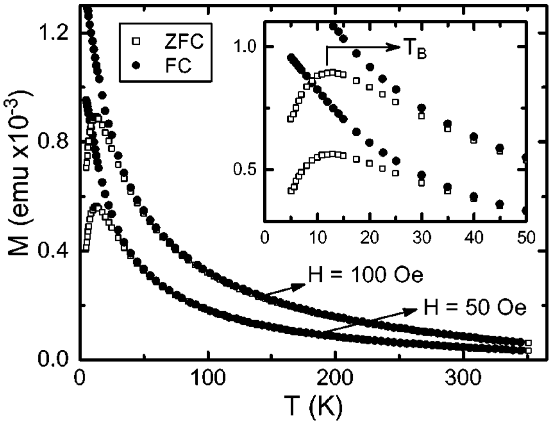

FIG. 4. Temperature dependence of the magnetization measured under both field cooled (FC) and zero-field cooled (ZFC) processes and applied magnetic fields of $H=50$ and 100 Oe for the C–Ni film with 22 wt % of Ni. The inset shows an expanded view of the low temperature region.

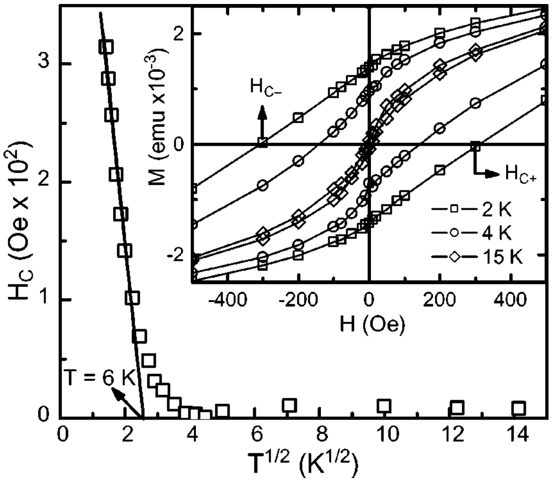

FIG. 5. Temperature dependence of the coercivity H_C of the C–Ni film with 22 wt % of Ni (squares). The line corresponds to a linear fit based on Eq. (2). The inset shows the low magnetic field region of the $M(H,T)$ curves measured at $T=2$, 4, and 15 K.

The blocking temperature of a system of randomly oriented, noninteracting particles can be roughly estimated by using the relationship

$$T_B = K\langle V\rangle/25k_B, \tag{1}$$

where $K=K_1^{\text{bulk}}=-8.5\times 10^4$ J/m^3 is the anisotropy constant of the bulk Ni, $\langle V\rangle$ is the average volume, and k_B is the Boltzmann constant.[15] Conversely, the above relationship can be useful to estimate the radius r_{TB} if Ni NPs are assumed to be spherical. Thus, by using the experimental value of $T_B=13$ K obtained from ZFC curves, a $r_{\text{TB}}=2.4$ nm is estimated. Such a value is in excellent agreement with the one of the HRTEM analysis shown in Fig. 3 ($r_{\text{TEM}}=2.3\pm 0.2$ nm).

To further confirm the transition to a blocked state below $T_B\sim 13$ K we have measured the magnetic field dependence $M(H,T)$ of the magnetization at different temperatures between 2 and 300 K. From typical results of these $M(H,T)$ measurements, shown in an expanded view in the inset of Fig. 5, one observes that coercivity remains essentially zero from room temperature down to $T_B\sim 13$ K, and develops appreciably below T_B. The $M\times H$ cycles taken after field cooling the samples from room temperature down to $T<T_B$, showed the absence of shift towards negative fields that characterizes an exchange-coupled system, as has been observed in metallic nanoparticles with shell (NiO)–core (Ni) morphology.[16,17]. Moreover, we have also found that the values of the coercivity fields measured under both increasing (H_{C+}) and decreasing fields (H_{C-}) are the same within the uncertainty limits of the procedure employed to determine H_C (~2 Oe). Such a result constitutes additional evidence for the absence of NiO surface layers in the Ni NPs, as inferred from the XPS data discussed above. If oxide surface layers were present an appreciable difference in the magnitudes of H_{C+} and H_{C-} would arise due to the exchange bias, as observed in metallic nanoparticles with shell (NiO)–core (Ni) morphology.[16,17] By computing the coercivity field H_C (H_{C+} or H_{C-}) at several different temperatures, we were able to build a H_C versus $T^{1/2}$ phase diagram, as shown in Fig. 5. The observed behavior indicates a thermally activated process with H_c increasing linearly with $T^{1/2}$ mainly at temperatures below ~6 K, as inferred from the extrapolated value of $T^{1/2}$ for $H_c=0$ (see Fig. 5). Such temperature dependence of H_C is the expected behavior for systems comprised of randomly oriented and noninteracting nanoparticles and is given by[15]

$$H_C(T) = H_{C0}[1-(T/T_B)^{1/2}], \tag{2}$$

with $H_{C0}=0.64\, K_1^{\text{bulk}}/M_S$,[18] where K_1^{bulk} is the anisotropy constant of bulk Ni described above, M_S is the saturation magnetization, and T_B is given by Eq. (1).

By using Eq. (1) and the value of $T_B=6$ K, we have found that the average radius r_{H_c} of the Ni nanoparticles is close to $r_{H_c}=1.9$ nm. This value agrees well with $r_{\text{TEM}}=2.3\pm 0.2$ nm, extracted from HRTEM images. Small differences between these estimated r values are certainly related to dipolar interactions between Ni NPs, a behavior expected in a film with 22 wt % of Ni. The extrapolated $H_C(0)\sim 730\pm 30$ Oe, inferred from the data shown in Fig. 5, is also of interest. By assuming the appropriate expression $H_C(0)=0.64$ K/M_S for randomly oriented and noninteracting particles and the Ni bulk value $M_S(T=0)=541$ emu/cm^3, one finds that $H_C(0)$ for Ni nanoparticles is close to 950 Oe. Such a zero-temperature coercivity field is higher, but comparable, to the one of ~730 Oe for the nanocomposite Ni–C film by the extrapolation of the H_C versus $T^{1/2}$ curve. The difference of ~25% between the predicted and the lower experimental coercivity extrapolated to $T=0$ K can be related to several mechanisms. These include an incoherent magnetization reversal processes related to weak interactions such as fanning and curling, which are expected to decrease H_{C0}.[19] These processes are frequently observed in patterned materials such as nanometric Ni chains and wires,[20,21] whereby incoherent rotation by curling is believed to reduce the reversing field down to ~30% of the value calculated for rotation in unison. However, due to the appreciable Ni concentration of 22 wt %, it seems that the reduction of H_{C0} would be related to dipolar interactions between Ni nanoparticles. Such interaction induces an evolution of the magnetization reversal toward more incoherent and heterogeneous mechanisms, thus reducing H_{C0} appreciably. On the other hand, the deviation from the spherical shape of the Ni NPs deduced from the HRTEM image analysis can also be related to a H_{C0} value different from the one calculated for spherical particles. Thus, it seems that the deviation of H_{C0} from the expected value would be related to both dipolar interactions between Ni NPs and shape anisotropy of individual nanoparticles.

We have also measured $M\times H$ curves at several temperatures ranging from 100 and 300 K, i.e., at temperatures well above $T_B\sim 13$ K and below the ferromagnetic transition temperature of bulk Ni of $T_c\sim 625$ K. Selected $M\times H$ curves are depicted in Fig. 6. In this figure, the data are collapsed into a universal curve of normalized magnetization M/M_S versus H/T. It is important to emphasize that the results in Fig. 6 represent only the magnetic signal arising from the Ni nanoparticles, since other magnetic contributions, originating from the Si substrate and the *a*-C matrix,

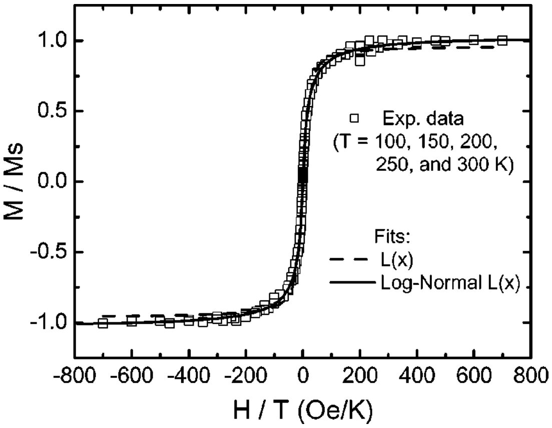

FIG. 6. Normalized magnetization as a function of H/T at temperatures of 100, 150, 200, 250, and 300 K for the C7–Ni film with 22 wt % of Ni (symbols). The results of the fittings of the $M\times H$ curves based on the simple $L(x)$ and the log-normal weighted Langevin functions are also shown (lines).

were subtracted. This was accomplished by an accurate measurement of the magnetic contribution of a blank sample, having similar weight and geometry, consisting of a pure *a*-C film deposited in a Si substrate taken from the same batch as the substrates used in the measured samples. The scaling shown in Fig. 6 is a well known feature of the SPM response, and can only be considered a true scaling at relatively low magnetic fields and temperatures above T_B. However, we have performed the scaling by assuming that contributions arising from SPM Ni NPs above T_B can be described by

$$M = M_s L(x), \tag{3}$$

where $M_s = N\mu$ is the saturation magnetization due to N nanoparticles with magnetic moment μ, and $L(x)$ is the Langevin function with argument $x=\mu H/k_B T$. Equation (3) is valid for systems comprised of noninteracting and monodisperse nanoparticles.

Moreover, based on the HRTEM results (see Figs. 2 and 3), the magnetization of SPM nanoparticles is expected to be better reproduced by considering a weighted sum of Langevin functions that takes into account a distribution of magnetic moments due to the particle size distribution[13,22]

$$M = \int_0^\infty L\left(\frac{\mu H}{k_B T}\right) f(\mu) d\mu, \tag{4}$$

where $f(\mu)$ is the distribution function of magnetic moments related to the saturation magnetization by

$$M_S = \int_0^\infty f(\mu) d\mu. \tag{5}$$

In the set of equations described above a temperature independent M_S is assumed, a condition valid provided that $T_B \ll T \ll T_C$. Therefore, the analysis is restricted to the temperature range from 100 to 300 K. Thus, in order to adjust the M/M_s versus H/T curves shown in Fig. 6, we have assumed a log-normal distribution $f(\mu)$ of magnetic moments given by[5]

$$f(\mu) = \frac{1}{\sqrt{2\pi}\mu\sigma} \exp\left(\frac{\ln^2(\mu/\mu_0)}{2\sigma^2}\right), \tag{6}$$

where σ is the distribution width and μ_0 is the median of the distribution related to the average (mean) magnetic moment μ_m by $\mu_m = \mu_0 \exp(\sigma^2/2)$.

The results of the fitting procedures, by assuming both simple and log-normal weighted Langevin functions, are shown in Fig. 6 for five different temperatures $T=100$, 150, 200, 250, and 300 K. The best fit based on the log-normal weighted Langevin functions was obtained by considering a median of the distribution $\mu_0 = 1.42\times 10^{-17}$ emu. This value corresponds to Ni nanoparticles comprised of ~2500 atoms, with a median radius $r_0 = 1.9$ nm, and a distribution width $\sigma = 1.15$. These values were used to estimate the mean radius of supposed spherical particles $r_m = 2.4$ nm. The result is in excellent agreement with the HRTEM analysis of $r_{\text{TEM}} = 2.3 \pm 0.2$ nm, as can be inferred from the data shown in Fig. 3. In fact, we have used the distribution of magnetic moments to generate a size distribution by assuming spherical particles, as shown in Fig. 3. One can see the good agreement between both distributions, thus lending credence to our analysis. On the other hand, the utilization of a simple $L(x)$ function resulted in a poorer fitting of the experimental data (see Fig. 6) and an estimated radius $r_{\text{L}} = 2.0$ nm, close to the median r_0 value.

We have also investigated the dynamical magnetic properties of the films by means of ac magnetic susceptibility $\chi_{\text{ac}}(T,f)$ as shown in Fig. 7. This figure displays both the real $\chi'(T)$ and imaginary $\chi''(T)$ components of the ac magnetic susceptibility $\chi_{\text{ac}}(T,f)$ for the film with 22 wt % of Ni. A careful inspection of the data indicates that both components exhibit a rounded maximum at $T_B \sim 13$ K, in agreement with dc magnetization data shown in Fig. 4. The results also reveal a feature frequently observed in several systems comprised of magnetic nanoparticles: a pronounced shift of these maxima in both $\chi'(T)$ and $\chi''(T)$ components towards lower temperatures with decreasing applied frequencies. In order to discriminate the blocking transition from a freezing temperature T_f of a spin-glass-like system, the empirical parameter

$$\Phi = \frac{\Delta T_B}{T_B \Delta \log_{10}(f)} \tag{7}$$

can be used for a rough estimation of the mechanisms involved through the frequency dependence of T_B. Here, ΔT_B is the shift of the blocking temperature T_B for a $\Delta \log_{10}(f)$ frequency variation. The obtained value $\Phi = 0.012$, extracted from the $\chi''(T)$ data, provides additional evidence pointing towards a SPM blocking transition.[23,24] Moreover, it also indicates that strong interparticle interactions, which usually yield collective magnetic dynamics (i.e., a super spin-glass phase), are not present in our samples.[25]

To further assess the dynamic response of the magnetic nanoparticles we have determined the anisotropy energy barrier E_a by fitting the experimental temperature dependence of the applied frequency with the Néel–Arrhenius law

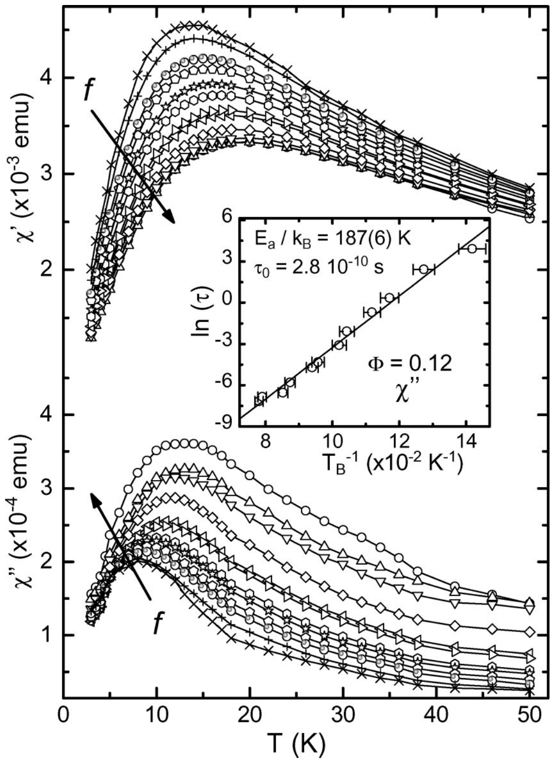

FIG. 7. Temperature dependence of the real $\chi'(T)$ and imaginary $\chi''(T)$ components of the ac magnetic susceptibility at different excitation frequencies for the film C–Ni with 22 wt % of Ni. (Inset) Arrhenius plot of the relaxation time τ versus blocking temperature T_B obtained from the imaginary component $\chi''(T)$ of the ac magnetic susceptibility. The solid line is the best fit using Eq. (8). The data were taken with an external magnetic field H of 50 Oe.

$$\tau = \tau_0 \exp\left(\frac{E_a}{k_B T}\right), \tag{8}$$

where τ_0 is in the 10^{-9}–10^{-11} s range for SPM systems. The energy barrier for a single domain particle, in zero external magnetic field, is usually assumed to be proportional to the particle volume V, $E_a = K_{\mathrm{eff}}$, V where K_{eff} is an effective anisotropy constant. It can be seen from the inset of Fig. 7 that the expected linear dependence of $\ln(f)$ versus T_B^{-1} is followed within a good approximation and the best fitting parameter $E_a = 2.6 \times 10^{-21}$ J $[E_a/k_B = 187(6\ \mathrm{K})]$ is obtained. Using the average particle size from TEM images $r_{\mathrm{TEM}} \sim 2.3$ nm, an effective anisotropy constant value $K_{\mathrm{eff}} = 5.1 \times 10^4$ J/m^3 was obtained. This effective value is related to the first-order magnetocrystalline anisotropy constant K_1 of cubic Ni through $K_{\mathrm{eff}} = K_1/12$,[26] thus yielding $K_1 = 6.1 \times 10^5$ J/m^3, a value slightly higher than the one corresponding to bulk Ni of $K_1^{\mathrm{bulk}} = 8.5 \times 10^4$ J/m^3.

Contributions to the energy barrier E_a can originate from the intrinsic anisotropy of the particles (shape, magnetocrystalline, or stress anisotropy), and also from interparticle interactions (dipolar or exchange). As described above, HRTEM images indicated a maximum in the elongation distribution close to 1.2. This deviation from the assumed spherical shape accounts for, at least, an increase in the anisotropy constant by a factor of 2. Moreover, it has been previously reported that a concentration of magnetic particles as small as ~5 wt % of Ni is sufficient to yield interparticle interactions of dipolar origin, a feature mirrored in an increase of the energy barrier estimated from $\chi_{ac}(T,f)$ data.[27] As the present film has a 22 wt % of Ni, interparticle contributions to E_a are likely to be responsible for the remaining difference observed in our estimates of the anisotropy constant.

SUMMARY

In summary, carbon–nickel thin film nanocomposites with controlled Ni composition were produced by the ion beam cosputtering method. The Ni nanoparticles were found to be homogenously distributed within a disordered carbon matrix and have an average radius of ~2 nm. The size distribution of the Ni nanoparticles shows a rather narrow shape distribution and an elongation factor of ~1.2, confirming the nearly spherical geometry of the particles. No evidence of oxygen was found through x-ray photoemission spectroscopy data, suggesting that the amorphous carbon film is a suitable matrix to prevent the NPs from surface oxidation. The films present a superparamagnetic behavior with blocking temperature $T_B \sim 13$ K, which corresponds to a system comprised of spherical nanoparticles with radius of ~2.3 nm, in excellent agreement with high-resolution transmission electron microscopy analysis. Magnetic measurements also indicated that the Ni nanoparticles are free from an oxide NiO layer, in agreement with the XPS data. In addition, we have inferred that the anisotropy constant, extracted from the magnetic data, seems to be strongly dependent on both the interparticle interactions and the shape of the Ni nanoparticles.

ACKNOWLEDGMENTS

This work was partially supported by the Brazilian agency FAPESP. ASF is a FAPESP fellow. F.A., G.F.G, and R.F.J. are CNPq fellows. This research was partially performed at LNLS—Laboratório Nacional de Luz Sincrotron, Brazil.

[1] C. B. Murray, S. Sum, H. Doyle, and T. Betley, MRS Bull. **26**, 985 (2001).
[2] X. Nie, J. C. Jiang, E. I. Meletis, L. D. Tung, and L. Spinu, J. Appl. Phys. **93**, 4750 (2003).
[3] A. Gavrin and C. L. Chen, J. Appl. Phys. **73**, 6949 (1993).
[4] M. Klimenkov, J. von Borany1, W. Matz1, D. Eckert, M. Wolf, and K.-H. Müller, Appl. Phys. A: Mater. Sci. Process. **74**, 571 (2002).
[5] F. C. Fonseca, G. F. Goya, R. F. Jardim, N. L. V. Carreño, R. Muccillo, E. Longo, and E. R. Leite, Appl. Phys. A: Mater. Sci. Process. **76**, 621 (2003).
[6] C. A. Morris, M. L. Anderson, R. M. Stroud, C. I. Merzbacher, and D. R. Rolison, Science **284**, 622 (1999).
[7] Y. Lifshitz, Diamond Relat. Mater. **8**, 1659 (1999).
[8] K. I. Schiffmann, M. Fryda, G. Goerigk, R. Lauer, P. Hinze, and A. Bulack, Thin Solid Films **347**, 60 (1999).
[9] J. J. Delaunay, T. Hayashi, M. Tomita, and S. Hirono, Jpn. J. Appl. Phys., Part 1 **36**, 7081 (1997).
[10] D. Babonneau, J. Briatico, F. Petroff, T. Cabioc'h, and A. Naudon, J. Appl. Phys. **87**, 3432 (2000).
[11] P. Hammer, N. M. Victoria, and F. Alvarez, J. Vac. Sci. Technol. A **18**, 2277 (2000).
[12] J. C. Russ, *The Image Processing Handbook* (CRC, Boca Raton, Fl, 1992).
[13] E. F. Ferrari, F. C. S. da Silva, and M. Knobel, Phys. Rev. B **56**, 6086 (1997).

[14] F. C. Fonseca, G. F. Goya, R. F. Jardim, N. L. V. Carreño, R. Muccillo, E. Longo, and E. R. Leite, Phys. Rev. B **66**, 104406 (2002).

[15] E. C. Stoner and E. P. Wohlfarth, Philos. Trans. R. Soc. London, Ser. A **240**, 599 (1948).

[16] M. Fraune, U. Rudiger, G. Guntherodt, S. Cardoso, and P. Freitas, Appl. Phys. Lett. **77**, 3815 (2001).

[17] Y. D. Yao, Y. Y. Chen, M. F. Tai, D. H. Wang, and H. M. Lin, Mater. Sci. Eng., A **217**, 837 (1996).

[18] R. M. Bozorth, *Ferromagnetism* (Van Nostrand, Princeton, N.J., 1956), Chap. 18, p. 831.

[19] J. B. D. Cullity, *Introduction to Magnet* (Addison-Wesley, Reading, MA, 1972), Chap. 11.

[20] P. M. Paulus, F. Luis, M. Kröll, G. Schmid, and L. J. de Jongh, J. Magn. Magn. Mater. **224**, 2 (2001).

[21] J. I. Martín, J. L. Costa-Kramer, F. Briones, and J. L. Vicent, J. Magn. Magn. Mater. **221**, 215 (2000).

[22] J. C. Cezar, M. Knobel, and H. C. N. Tolentino, J. Magn. Magn. Mater. **226–230**, 1519 (2001).

[23] J. L. Dormann, D. Fiorani, and E. Tronc, in *Advances in Chemical Physics*, edited by I. Prigogine and S. A. Rice (Wiley, New York, 1997), Vol. XCVIII, p. 326.

[24] J. A. Mydosh, *Spin Glasses: An Experimental Introduction* (Taylor & Francis, London, 1993), Chap. 3.

[25] C. Djurberg, P. Svedlindh, P. Nordblad, M. F. Hansen, F. Bødker, and S. Mørup, Phys. Rev. Lett. **79**, 5154 (1997).

[26] J. I. Gittleman, B. Abeles, and S. Bozowski, Phys. Rev. B **9**, 3891 (1974).

[27] G. F. Goya, F. C. Fonseca, R. F. Jardim, R. Muccillo, N. L. V. Carreño, E. Longo, and E. R. Leite, J. Appl. Phys. **93**, 6531 (2003).